Efficient Interfacial Electrons Transfer Induced by Hollow-Structured $ZnIn_2S_4$ Extending Hot Electrons Lifetimes

Yuchen Guo[a], Jiaming Sun[c], Yuan Tang[a], Xiaofang Jia[c], Yu Nie[a], Zikang Geng[b], Chunyang Wang[b], Junying Zhang[c*], Xin Tan[a], Dichang Zhong[e], JinhuaYe[d*], Tao Yu[b*]

[a]School of Environmental Science and Engineering, Tianjin University, Tianjin 300350, P. R. China

[b]School of Chemical Engineering and Technology, Tianjin University, Tianjin 300350, P. R. China

[c]School of Physics, Beihang University, Beijing 100191, P. R. China

[d]International Center for Materials Nanoarchitectonics (WPI-MANA) National Institute for Materials Science (NIMS), 1-1 Namiki, Tsukuba 305-0047, Japan

[e]MOE International Joint Laboratory of Materials Microstructure, Institute for New Energy Materials and Low Carbon Technologies, School of Materials Science and Engineering, Tianjin University of Technology, Tianjin 300384, P. R. China

*Corresponding Author

E-mail address:

yutao@tju.edu.cn (T. Yu)

zjy@buaa.edu.cn (J. Y. Zhang)

jinhua.ye@nims.go.jp (J. H. Ye)

Table of Contents

4. Experimental Section

4.1. Chemicals and reagents

Zinc nitrate ($Zn(NO_3)_2·6H_2O$), 2-methylimidazole (2-MeIm), methanol, tannic acid (TA), zinc chloride ($ZnCl_2$), indium chloride ($InCl_3$), thioacetamide (TAA), glycerol, nickel nitrate hydrate ($Ni(NO_3)_2·6H_2O$), cobalt nitrate hydrate ($Co(NO_3)_2·6H_2O$), thiourea (CH_4N_2S) ethylene glycol, alcohol and ascorbic acid were of analytical grade and used without further purification.

4.2. Synthesis of ZIF-8 and yolk-shelled ZIF-8

In a typical experimental procedure, 8 mmol $Zn(NO_3)_2·6H_2O$ and 16 mmol 2-MeIm were dissolved in 100 mL of methanol to form solution A and B. Then, the solution B was slowly added dropwise to solution A under magnetic stir. The mixture solution was aged for 12 h at room temperature without stirring. Finally, the white products were collected by centrifugation, washed with absolute ethanol several times, and dried in a vacuum oven at 60 °C overnight to obtain ZIF-8.

The yolk-shelled ZIF-8 (ZIF-8-YS) was prepared via a tannic acid etching procedure. Typically, 40 mg as-prepared ZIF-8 were dispersed into a methanol solution of TA (200 mL, 5 g L^{-1}). Subsequently, the obtained mixture was vigorously stirred for 30 minutes, and the products were collected by centrifugation, washed with absolute ethanol several times for further use.

4.3. Synthesis of hollow $ZnIn_2S_4$ nanocages

In order to synthesize the hollow $ZnIn_2S_4$ nanocages, the as-prepared ZIF-8-YS was first scattered into 14 mL of alcohol and sonicated for 5 min to form solution A

while 54.4 mg $ZnCl_2$, 117.2 mg $InCl_3$ and 60 mg TAA were dissolved in a mixture solution composed of 10 mL of alcohol and 6 mL of glycerol to form solution B. Subsequently, solution A was rapidly poured into solution B and continuously stirred for 30 min. Afterward, the above solution was transferred into 50 mL Teflon-lined autoclave and maintained at 180 °C for 2 h. Finally, the samples were collected by centrifugation, washed by deionized water and ethanol for several times and dried at 60 °C overnight. The obtained samples were named as ZIS-HNCs. In addition, the $ZnIn_2S_4$ nanocages with thick shell (labeled as ZIS-NCs) and bulk $ZnIn_2S_4$ (labeled as ZIS) were prepared under the same condition as ZIS-HNCs, except adding the original ZIF-8 as template and not adding any template agent.

4.4. Synthesis of $NiCo_2S_4$ and $NiCo_2S_4/ZnIn_2S_4$ composite

$NiCo_2S_4$ was prepared by one-step solvothermal method. Typically, 1 mmol $Ni(NO_3)_2 \cdot 6H_2O$, 2 mmol $Co(NO_3)_2 \cdot 6H_2O$, and 5 mmol thiourea were co-dissolved in 60 mL of ethylene glycol. After stirred for 30 min, the obtained solution was transferred into 100 mL Teflon-lined autoclave and maintained at 180 °C for 15 h. Finally, the black samples were collected by centrifugation, washed by deionized water and ethanol for several times and dried at 60 °C overnight. The obtained black samples were labeled as NCS briefly.

$NiCo_2S_4/ZnIn_2S_4$ composite was synthesized via a mechanical assembly procedure. In a typical procedure, 5 mg NCS and 100 mg ZIS-HNCs were added in an agate mortar and continued to grind for 5 min to prepare the composite named as NCS/ZIS-HNCs. Moreover, different amount (1mg, 10 mg and 100 mg) of NCS were

added to 100 mg ZIS-HNCs for preparing the composite. **Unless otherwise specified, the loading of NCS in the composites NCS/ZIS-HNCs mentioned in this study is 5 mg**.

4.5. Characterizations

The samples were analyzed by the X-ray diffractometer (XRD, D8-Focus Bruker, German). UV–vis absorption spectra were obtained by spectrophotometer (UV-3600, Shimadzu, Japan). Microstructure and morphology information were obtained by the field emission scanning electron microscopy (SEM, Regulus 8100, Japan) and transmission electron microscopy (TEM, JEM-F200, Japan). X-ray photoelectron spectroscopy (XPS, K-Alpha+, England) was used to demonstrate the chemical compositions and surface states. The working function was characterized by ultraviolet photoelectron spectroscopy (UPS) using a functional component equipped on XPS. Photoluminescence spectra (Hitachi F4500, Japan) was used to characterize steady-state photoluminescence (PL) and time-resolved photoluminescence (TRPL). Electron spin-resonance resonance (ESR, JES-FA 200, JEOL, Japan, 100 kHz, 1.0 mW) was performed at room temperature. Surface photovoltage spectroscopy (SPV) of as-prepared samples under dark and $\lambda > 420$ nm conditions were measured by the Kelvin probe force microscopy (KPFM) (Bruker Dimension icon, Germany), and the probe is SCM-PIT. Transient absorption spectra of samples were obtained using a commercial femtosecond pump-probe system (Helios, Ultrafast Systems). The output of an optical parametric amplifier (Opera Solo, Coherent) coupled with 800 nm, 1 kHz amplified Ti: sapphire laser system (Astrella, Coherent) was used as the pump beam (100 fs). The

wavelength was scanned from 430 to 770 nm. The pump beam was modulated by a mechanical chopper at a frequency of 500 Hz. The transmitted probe pulses were collected by photodiode arrays and recorded one by one. The lifetimes were obtained by fitting TAS curves with exponential decay function using Origin 2023. The surface temperatures of samples were measured with infrared thermal imager (Smart Sensor, ST9450).

4.6. Photocatalytic measurement

The photocatalytic measurement was carried out in a vacuum system (Shanghai Boyi Scientific Instrument Co. Ltd., China) while irradiated with a 300 W Xe lamp ($\lambda >$ 420 nm, Newbit, China), and the reaction current was set as 20.0 A. The mass of photocatalyst for photocatalytic hydrogen evolution rate has been optimized, the detail information is exhibited in **Figure S37**. In a typical method, 20 mg of prepared photocatalyst powder was added in a reaction cell containing 270 mL aqueous solution of 0.1M ascorbic acid sacrificial agent, which the pH was measured at 2.78. Before irradiation, reaction system was vacuumized for 30 min to remove residual gases. The hydrogen quantity was measured by an on-line gas chromatograph (GC-2014AT 230 V R, Shimadzu Co., Japan). Information about vacuum system and photoreactor are exhibited in **Figure S38** to allow reproducibility.

For the calculation about apparent quantum efficiency (AQE), the AQE under different visible light was calculated with **Equation S1**:

$$\mathrm{AQE} = \frac{\text{number of reacted electrons}}{\text{number of incident photons}} \times 100\%$$

$$= \frac{\text{number of evolved H2 molecules} \times 2}{\text{number of incident photons}} \times 100\% \qquad \text{(S1)}$$

where the number of incident photons were measured by fiber optic spectrometer (AvaSolar-1, Avantes, USA). The measurement schematic diagram is exhibited in **Figure S39a**, the distance between the probe and the xenon lamp before the test was adjusted to the distance between the xenon lamp and the liquid surface during the photocatalytic reaction. The xenon lamp was equipped with bandpass filters of 400, 420, 450, 470, 500, 560, 650 and 750 nm (Newbit, China), respectively. During the measurement, five points were selected, measured and averaged (**Figure S39b**).

The apparent activation energy (E_a) was calculated according to the Arrhenius formula (**Equation S2**):

$$\ln k = -\frac{E_a}{RT} + \ln A \qquad \text{(S2)}$$

where k is reaction rate constant, R is molar gas constant, T is Kelvin temperature and A is pre-exponential factor. During the reaction, the temperature was maintained at 277, 281, 285 and 289 K by temperature-controlled water tank, respectively. The photoreactor with cooling water is exhibited in **Figure S40**.

For the 5-cycle stability experiment, after the photocatalytic hydrogen evolution was completed, the reaction device was re-evacuated to vacuum. The reacted solution containing the photocatalyst and sacrificial agent was kept in photoreactor with continuous stirring at 600 rpm to prevent the photocatalyst from agglomeration, while the photoreactors was covered with tin foil to avoid light exposure. After the fourth cycle, when the photocatalytic hydrogen evolution rate decreased significantly, the photoreactor was disassembled from the vacuum system and a certain quality of ascorbic acid was reinjected into the above solution until the pH value was equal to

2.78.

4.7. Photoelectrochemical measurements

Photoelectrochemical was measured by a three-electrode system electrochemical workstation (CHI660E, Shanghai Chenhua), in which 0.1M Na_2SO_4, Ag/AgCl and Pt wire was served as the electrolyte solution, reference electrode and counter electrode, respectively. To prepare working electrode, 10 mg of photocatalyst powder was ultrasonically vibrated for 30 min with mixed 50 μL of naphthol and 450 μL of ethanol. Next, 50 μL of the prepared mixture was painted on the ITO conductive glass and dried at 60 °C overnight. The EIS Nernst curve was measured in the frequency form 0.01 Hz to 1 kHz. The I-t curve was measured at a bias voltage of 0.5 V. The energy band structures of the prepared materials were calculated according to **Equation (S3-S4)**

$$E_{NHE} = E_{Ag/AgCl} + 0.197\ V \quad (S3)$$

$$E_{VB} = E_{CB} + E_g \quad (S4)$$

4.8. Computational details

In this work, density functional theory (DFT) calculations were performed with the Vienna ab initio simulation package (VASP).[1] The exchange-correlation potential was described by the generalized gradient approximation (GGA) function introduced by Perdew, Burke and Ernzerhof (PBE).[2] Ion cores were described with projector augmented wave (PAW).[3, 4] The cutoff energy was set to 450 eV. The lattice constants and atomic positions were fully relaxed until the atomic forces were smaller than -0.02 eV/Å. The energy convergence criterion for self-consistent electronic calculation was set to 1×10^{-4} eV. A gamma-centered 4×2×1 k-mesh grid in the Brillouin zone was

adopted for the integration of surface supercell models. A vacuum region of 15 Å along the z-direction was added to minimize the interaction between each slab model. The DFT-D3 including Becke-Jonson damping was utilized to correct the long-range dispersion.[5, 6] The calculation crystal plane of ZIS and NCS were selected as (001) and (111), respectively. The method to build the model of NCS/ZIS including six ZIS and eight NCS unit cells was the same as our published work.[7] All models were visualized in VESTA. The S vacancy is introduced under the Zn atom layer to compare the effect of the S vacancy on NCS/ZIS interfacial charge transfer. The change of Gibbs free energy for the hydrogen evolution reaction (HER) was calculated by the **Equation S5**:[8]

$$\Delta G_{*\mathrm{H}} = \Delta E + \Delta ZPE - T\Delta S \quad \text{(S5)}$$

where ΔE is the binding energy, ΔZPE is the difference in zero-point energies, and ΔS is the change of entropy, respectively. The Gibbs free energies of the reaction were modified by the contribution of the vibrational frequencies of the surface molecules to ΔZPE and entropy. The adsorption of H^+ by the NCS/V_S-ZIS slab is the transition state of HER process.

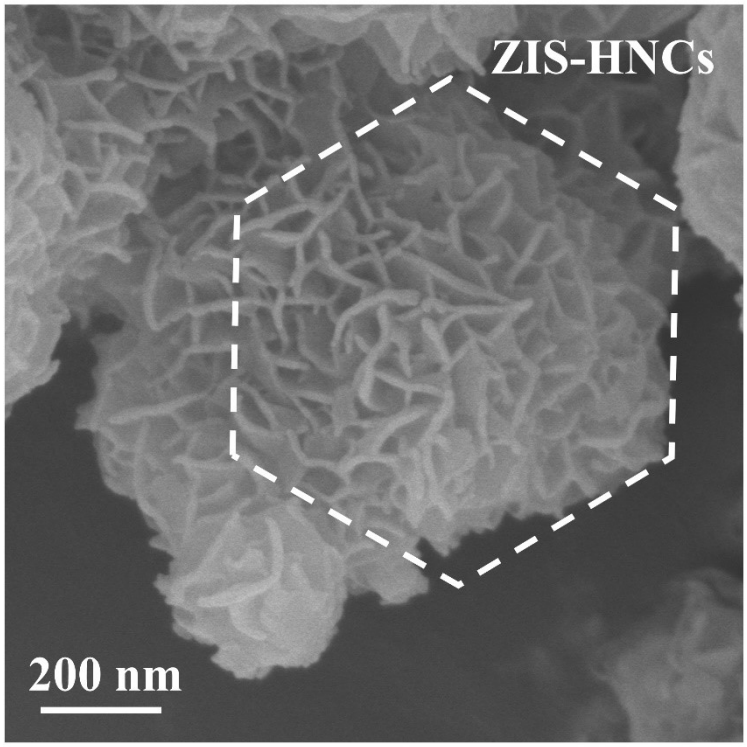

Figure S1. SEM image of ZIS-HNCs.

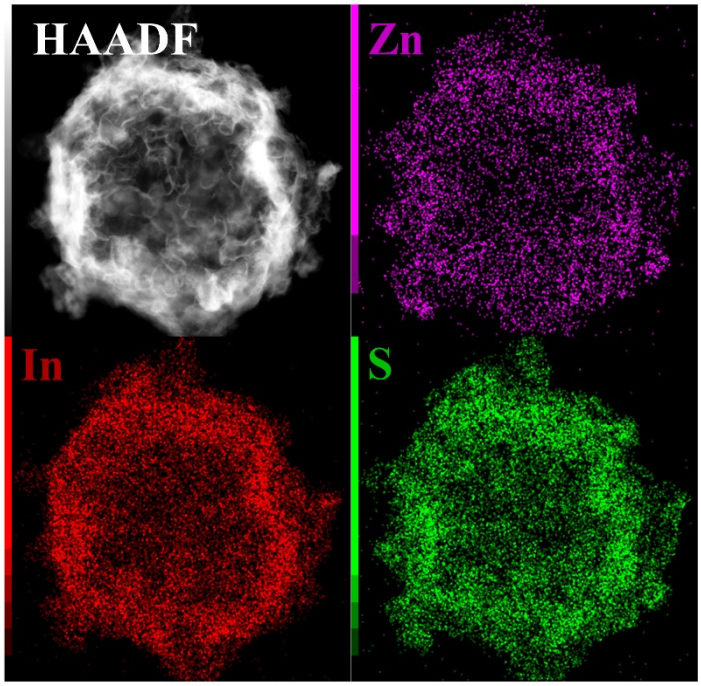

Figure S2. Elements mapping of ZIS-HNCs.

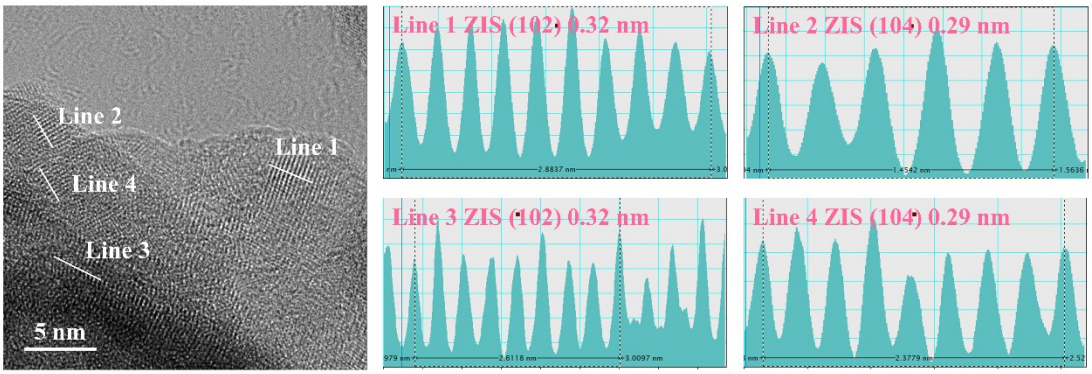

Figure S3. HRTEM image of ZIS-HNCs.

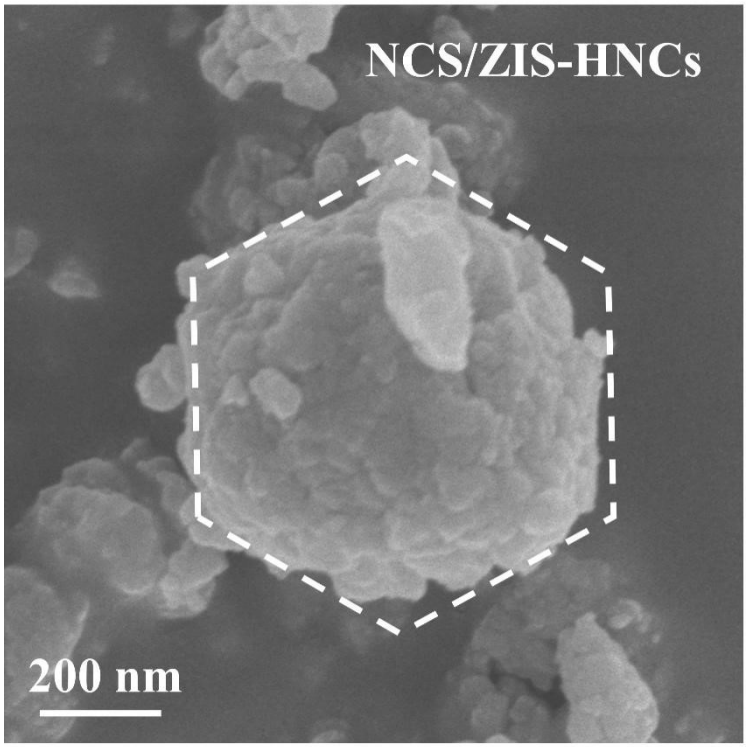

Figure S4. SEM image of NCS/ZIS-HNCs.

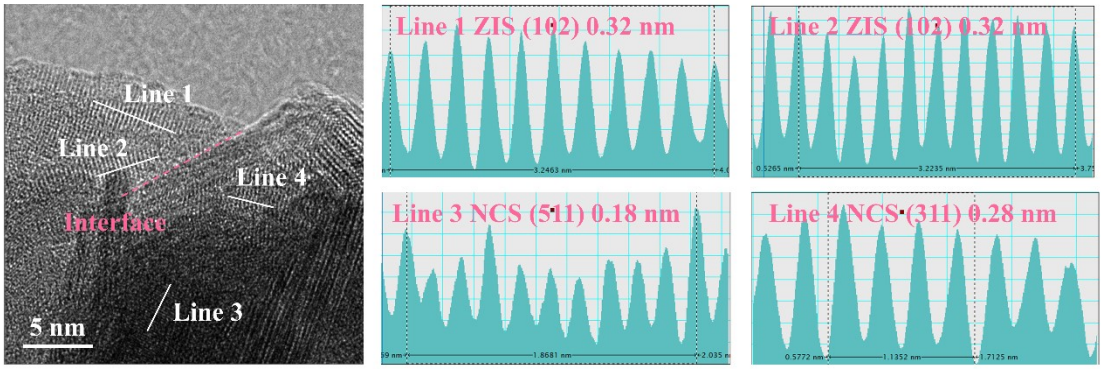

Figure S5. HRTEM image of NCS/ZIS-HNCs.

The different lattice fringes on two sides of the distinct interface with interplanar spacings of 0.32, 0.28 and 0.18 nm can be correlated with the (102) lattice plane of hexagonal $ZnIn_2S_4$ and the (311) and (511) crystal planes of $NiCo_2S_4$, respectively.

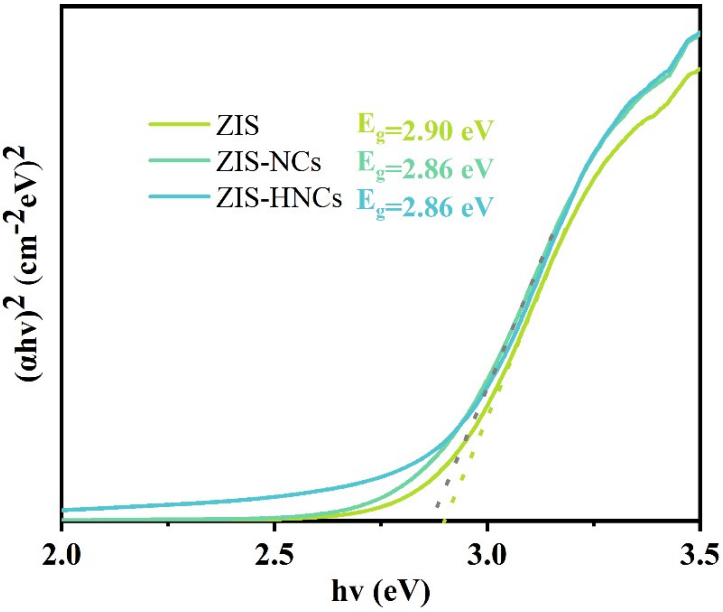

Figure S6. Band gap width of ZIS, ZIS-NCs and ZIS-HNCs.

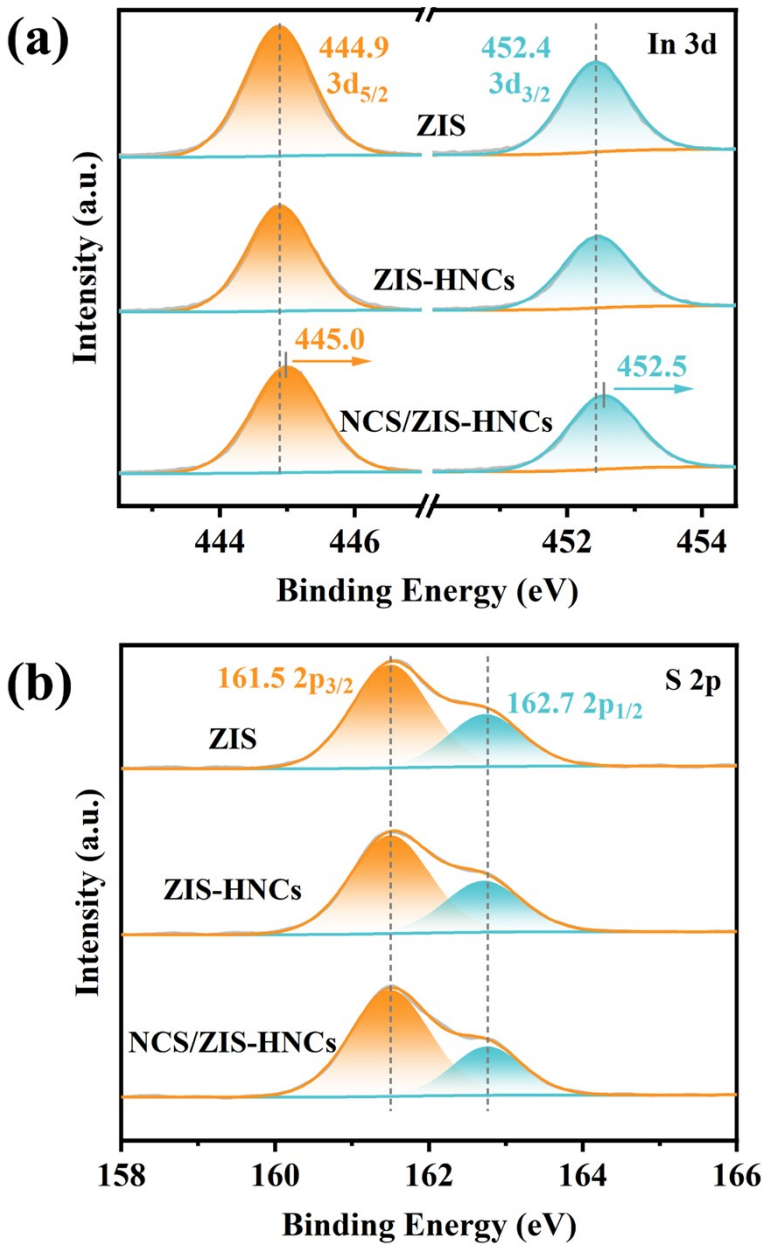

Figure S7. XPS spectra: (a) In 3d, (b) S 2p of ZIS, ZIS-HNCs and NCS/ZIS-HNCs.

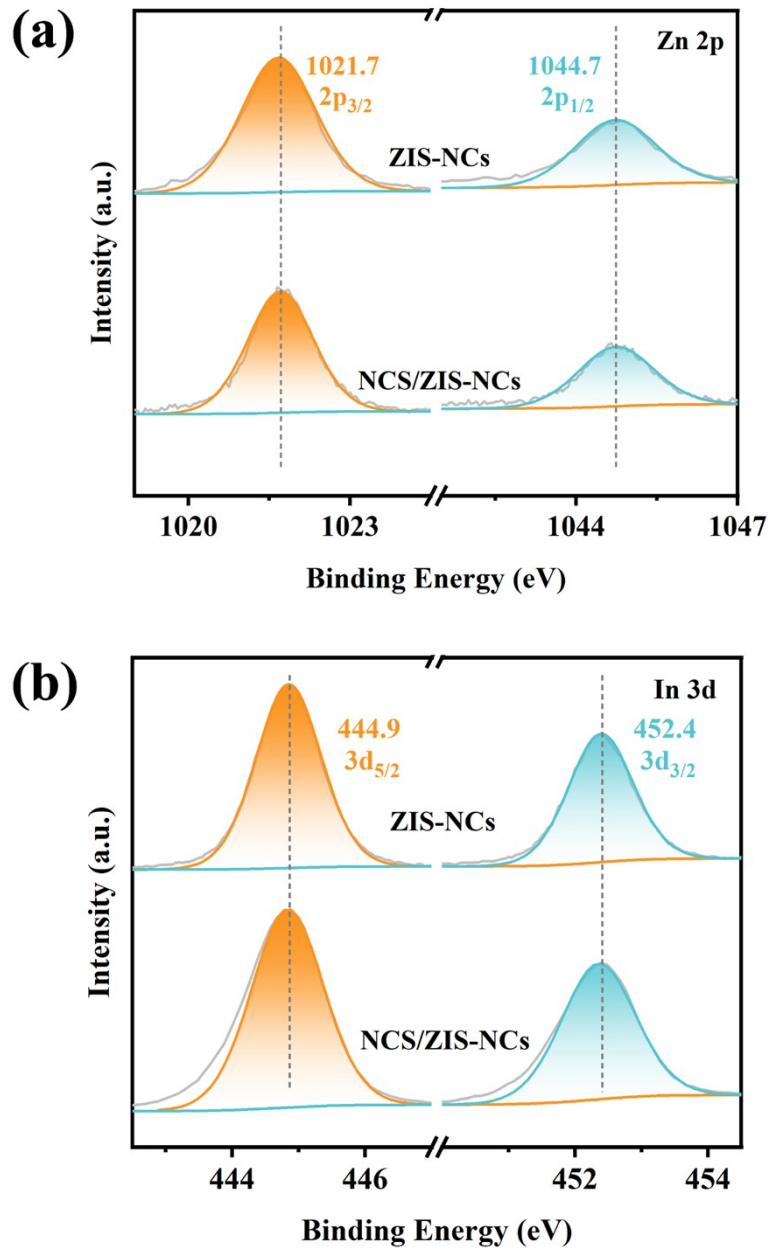

Figure S8. XPS spectra: (a) Zn 2p, (b) In 3d of ZIS-NCs and NCS/ZIS-NCs.

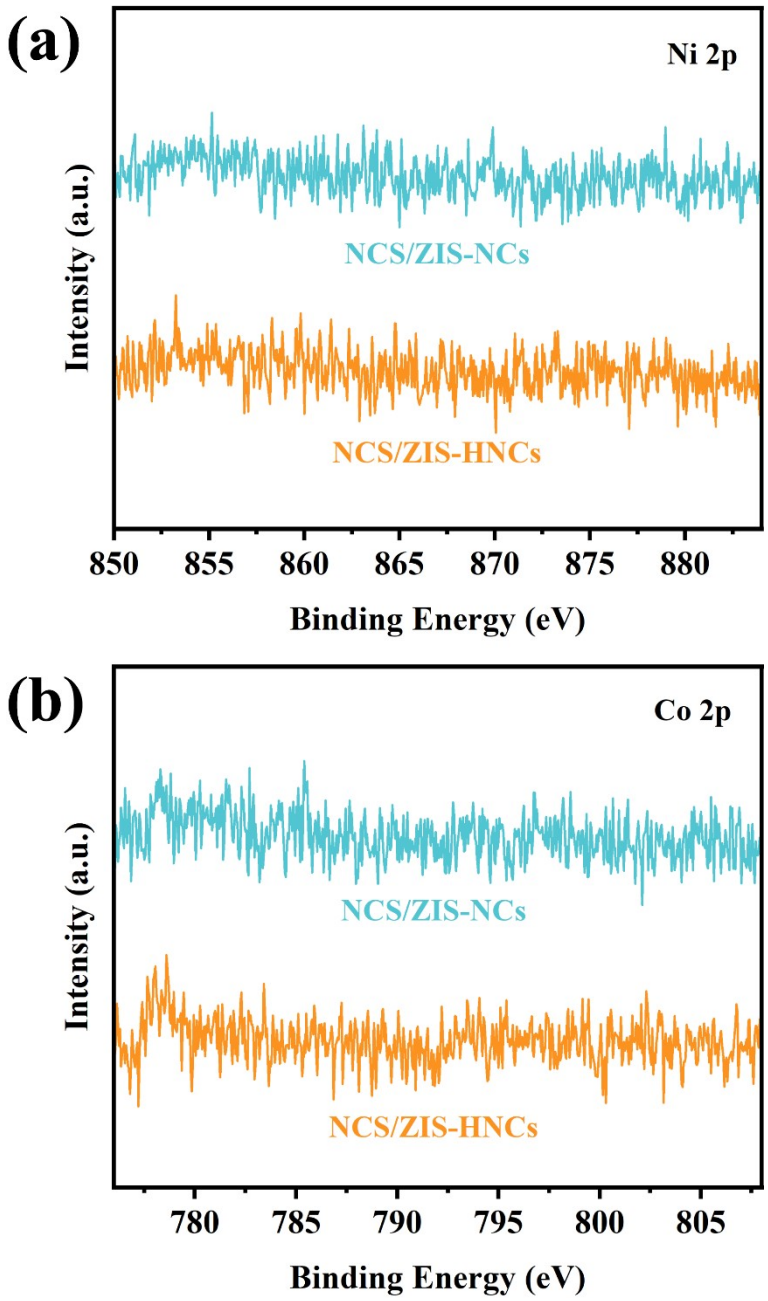

Figure S9. XPS spectra: (a) Ni 2p, (b) Co 2p of NCS/ZIS-NCs and NCS/ZIS-HNCs.

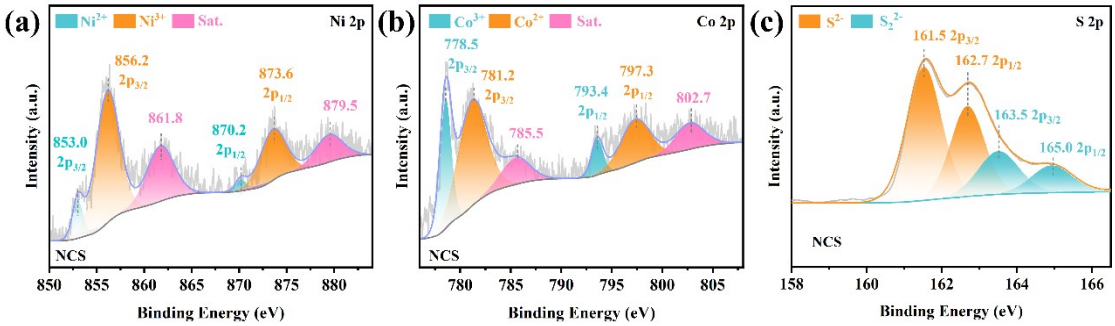

Figure S10. XPS spectra: (a) Ni 2p, (b) Co 2p, (c) S 2p of NCS.

The peaks at 853.0 and 870.2 eV were characteristics of the $2p_{3/2}$ and $2p_{1/2}$ of Ni^{2+}, and those at 856.2 and 873.6 eV were assigned to the $2p_{3/2}$ and $2p_{1/2}$ of Ni^{3+}(**Figure S10a**). The peaks at 778.5 and 793.4 eV were characteristics of the $2p_{3/2}$ and $2p_{1/2}$ of Co^{3+}, and those at 781.2 and 797.3 eV were assigned to the $2p_{3/2}$ and $2p_{1/2}$ of Co^{2+} (**Figure S10b**). The peaks at 161.5 and 162.7 eV were characteristics of the $2p_{3/2}$ and $2p_{1/2}$ of S^{2-}, and those at 163.5 and 165.0 eV were assigned to the $2p_{3/2}$ and $2p_{1/2}$ of the unsaturated S (S_2^{2-}) (**Figure S10c**).

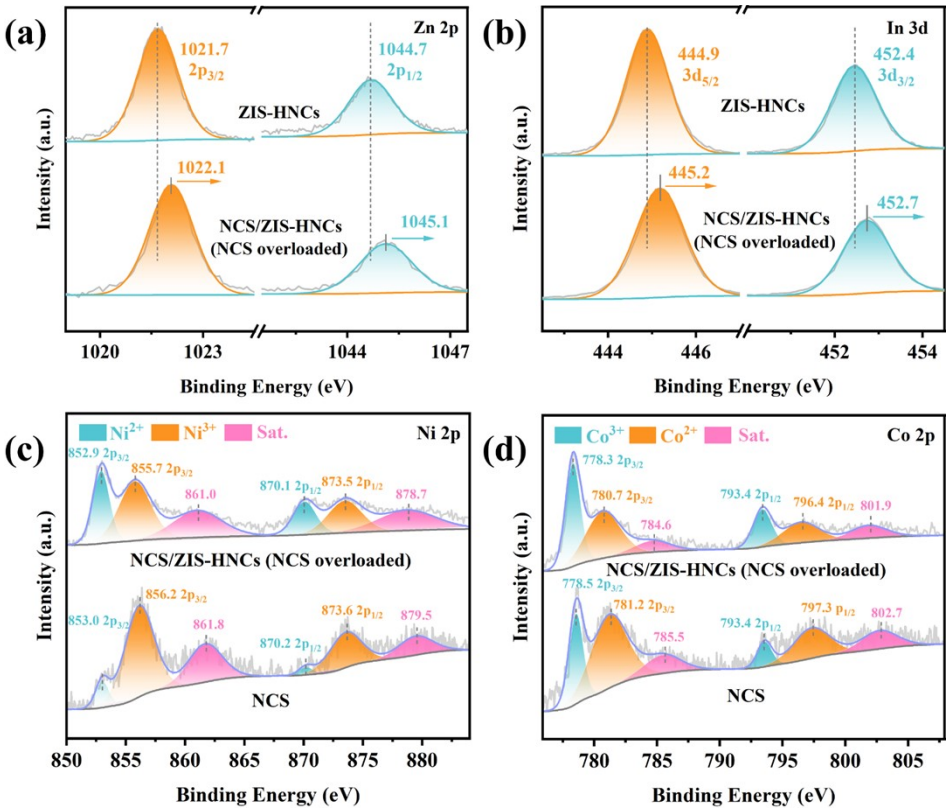

Figure S11. XPS spectra: (a) Zn 2p, (b) In 3d of ZIS-HNCs and NCS/ZIS-HNCs (NCS overloaded), (c) Ni 2p, (d) Co 2p of NCS/ZIS-HNCs (NCS overloaded) and NCS.

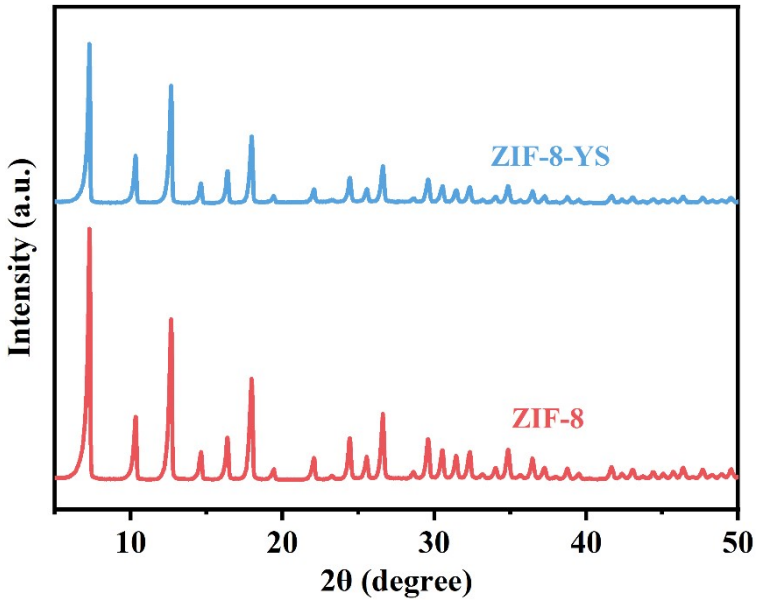

Figure S12. XRD patterns of ZIF-8 and ZIF-8-YS.

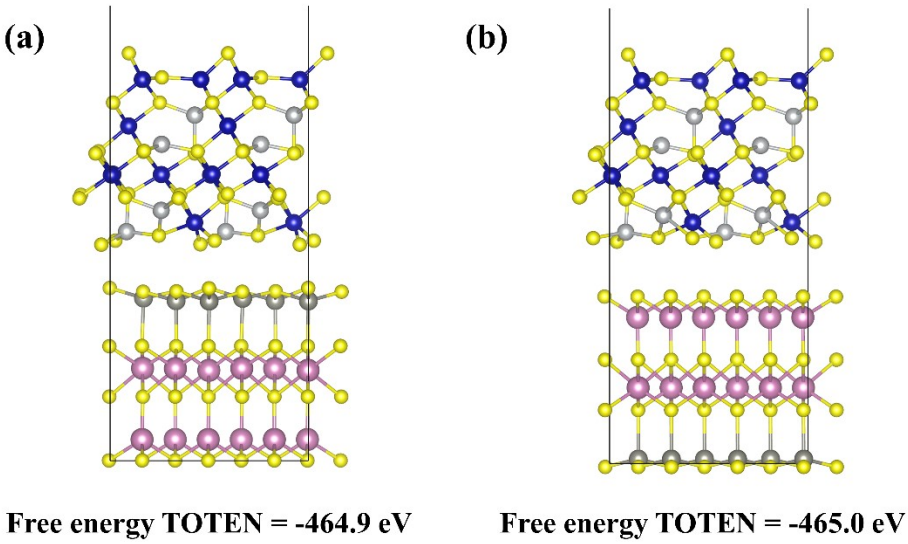

Figure S13. Total free energies of interface contact structure of (a) Zn-S layer terminated ZIS and (b) In-S layer terminated ZIS with NCS.

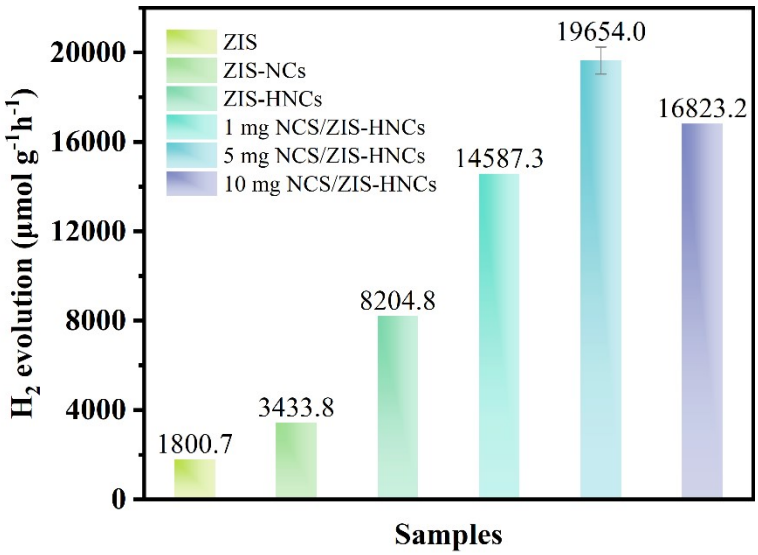

Figure S14. PHE rate of the as-synthesized samples.

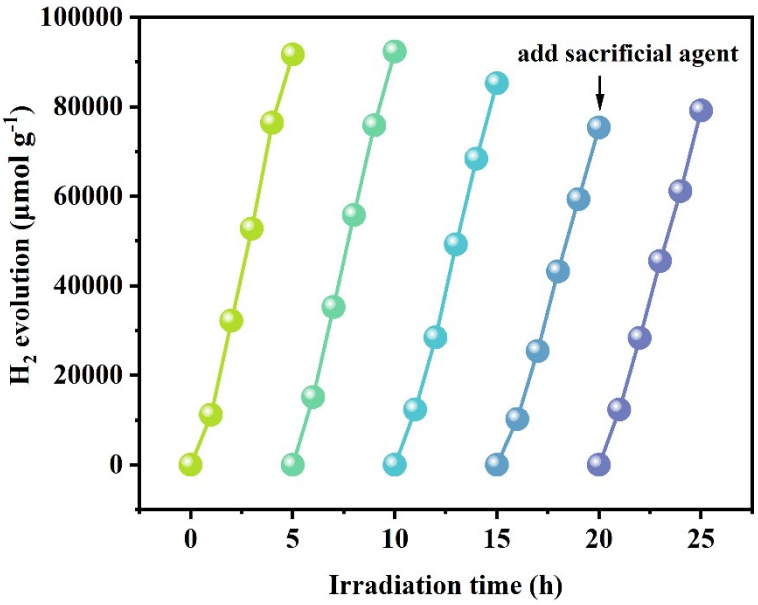

Figure S15. Cycling experiment of NCS/ZIS-HNCs.

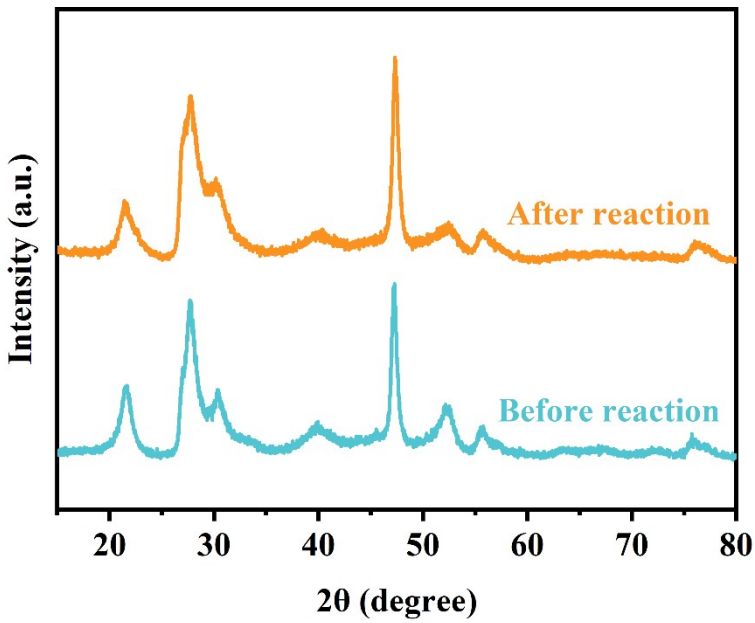

Figure S16. XRD patterns of NCS/ZIS-HNCs before reaction and after photocatalytic reaction.

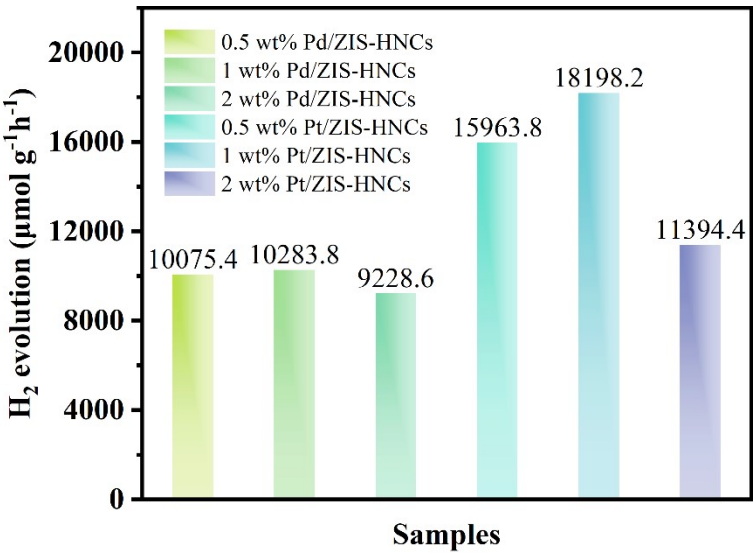

Figure S17. PHE rate of the as-synthesized samples.

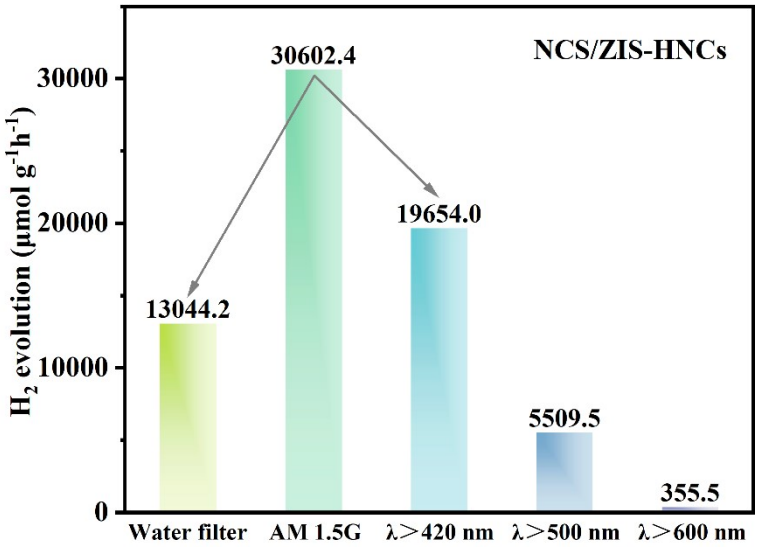

Figure S18. PHE rate of NCS/ZIS-HNCs under different-wavelength light irradiation and water filter.

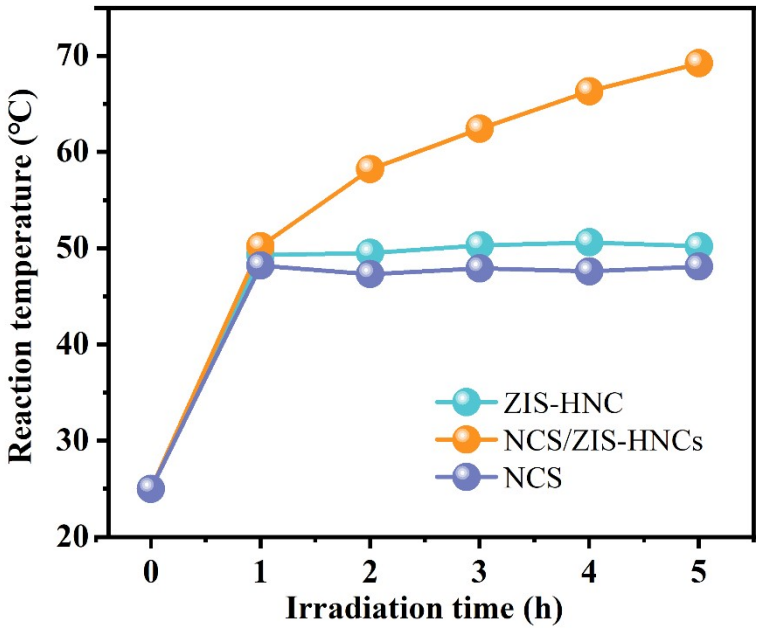

Figure S19. PHE temperature of as-synthesized samples.

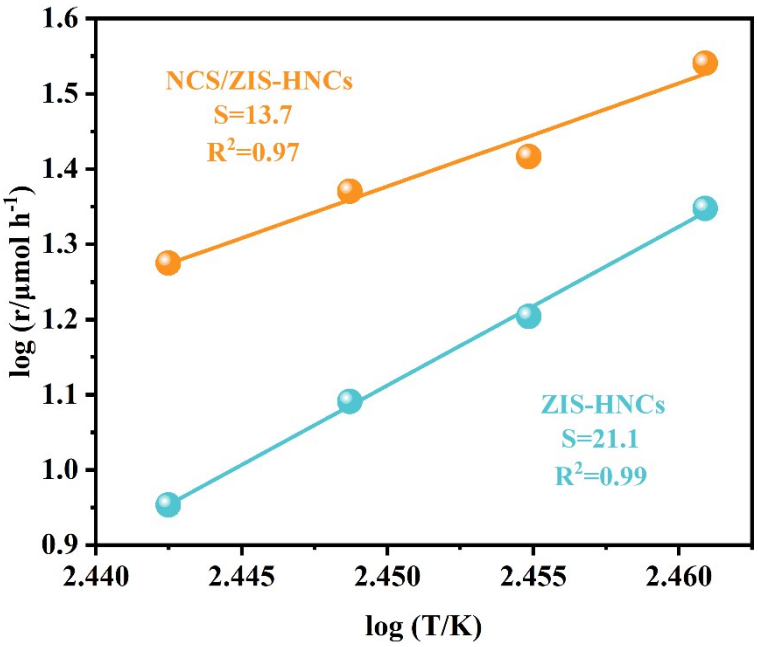

Figure S20. Relationships between the PHE rate on ZIS-HNCs and NCS/ZIS-HNCs and reaction temperature on a double logarithmic scale.

The experimental data measured at controlled temperature in **Figure S20** were used to calculate apparent activation energy in **Figure 3d**. Apparent activation energy is proportional to reaction order, and the reaction with low apparent activation energy is insignificantly affected by reaction temperature from macroscopical view to exhibit low reaction order. Consequently, NCS/ZIS-HNCs with low apparent activation energy exhibits lower reaction order than ZIS-HNCs with high apparent activation energy.

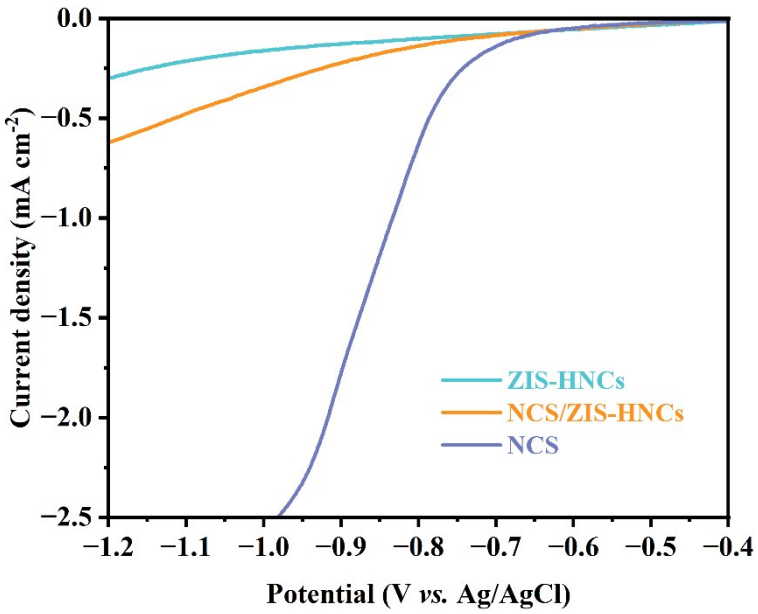

Figure S21. Linear sweep voltammetry (LSV) curves of ZIS-HNCs, NCS/ZIS-HNCs and NCS.

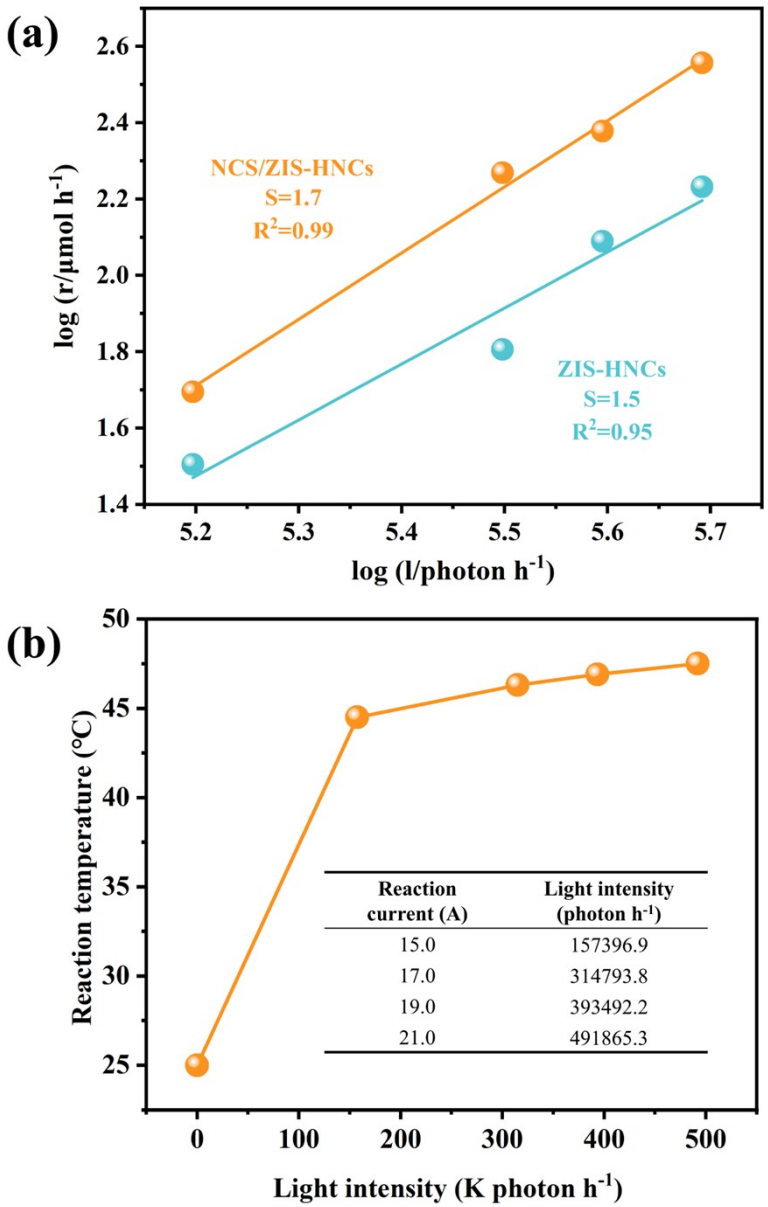

Figure S22. (a) Relationships between the PHE rate (λ > 420 nm) on ZIS-HNCs and NCS/ZIS-HNCs and light intensity on a double logarithmic scale, (b) Reaction temperature for blank experiment at different light intensity.

The reaction temperature for blank experiment at different light intensity exhibit a minor increase form 44.5 ℃ to 47.5 ℃ (**Figure S22b**). Both the light intensity and different light intensity induced temperature minor enhancement are external factors, which can influence the PHE rate on y-axis. However, the reaction order is calculated from the derivative of the line, which is influenced by internal factor. In this experiment, the enhanced reaction order on NCS/ZIS-HNCs is contributed by photothermal effect.

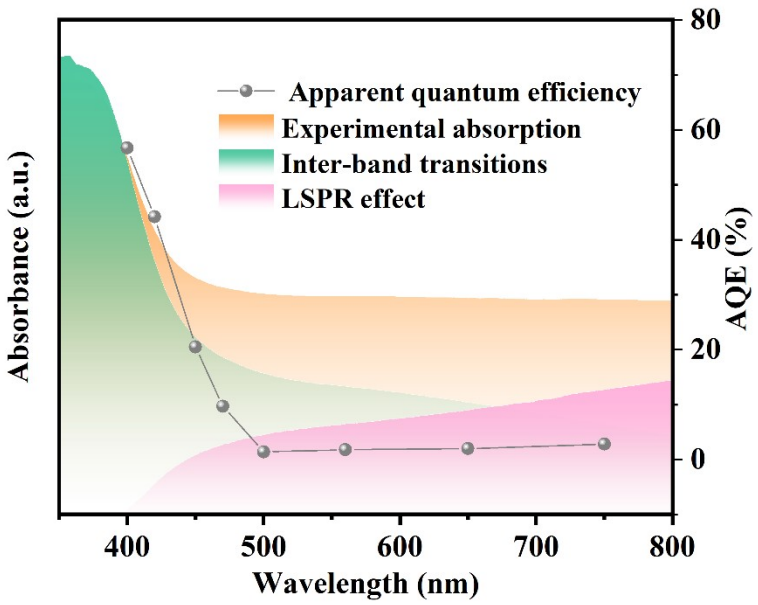

Figure S23. Contribution of inter-band transitions and LSPR effect at different wavelengths.

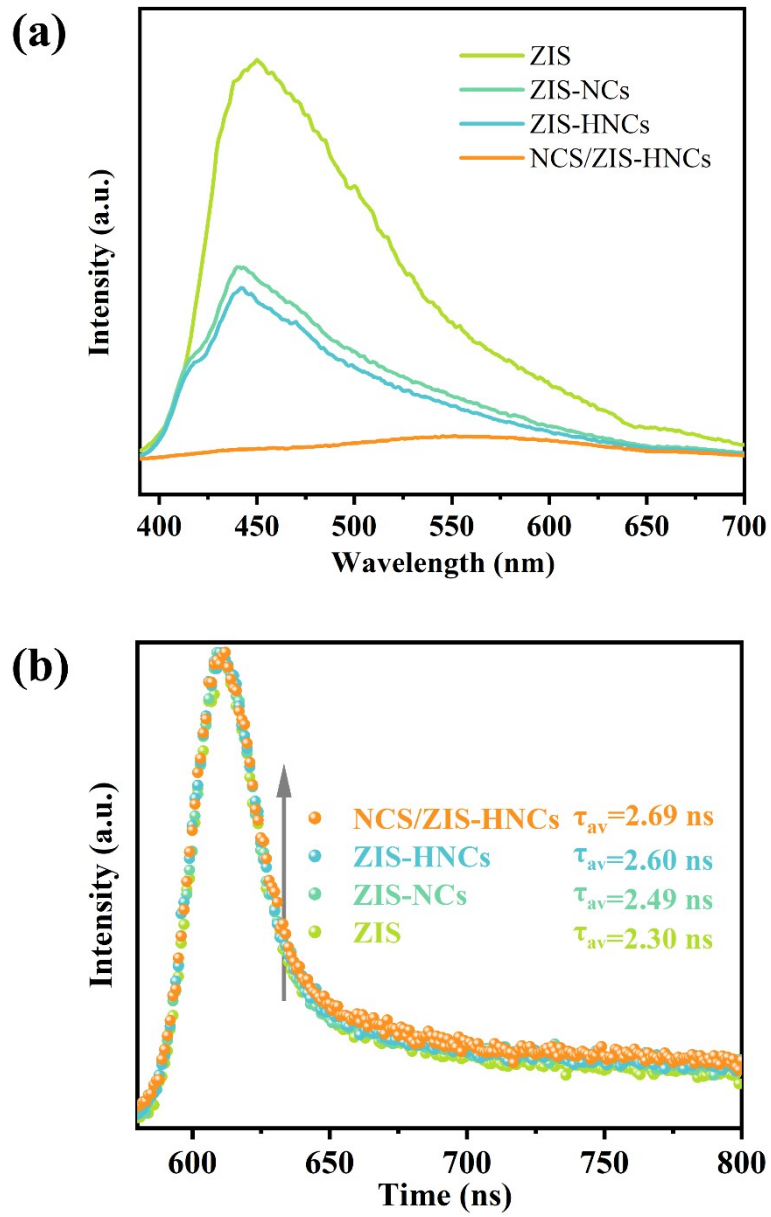

Figure S24. (a) PL spectra of the as-synthesized samples, (b) Transient fluorescence emission spectra of the as-synthesized samples.

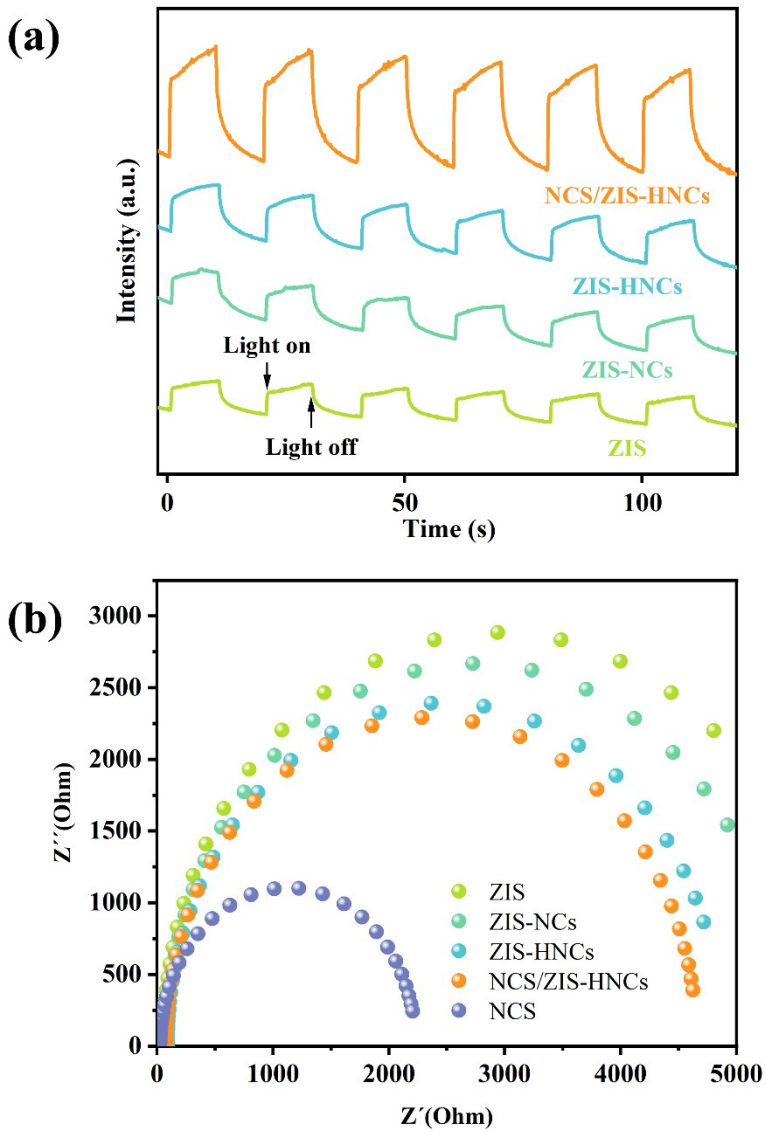

Figure S25. (a) Transient photocurrent response of the as-synthesized samples, (b) Electrochemical impedance spectra (EIS) of the as-synthesized samples.

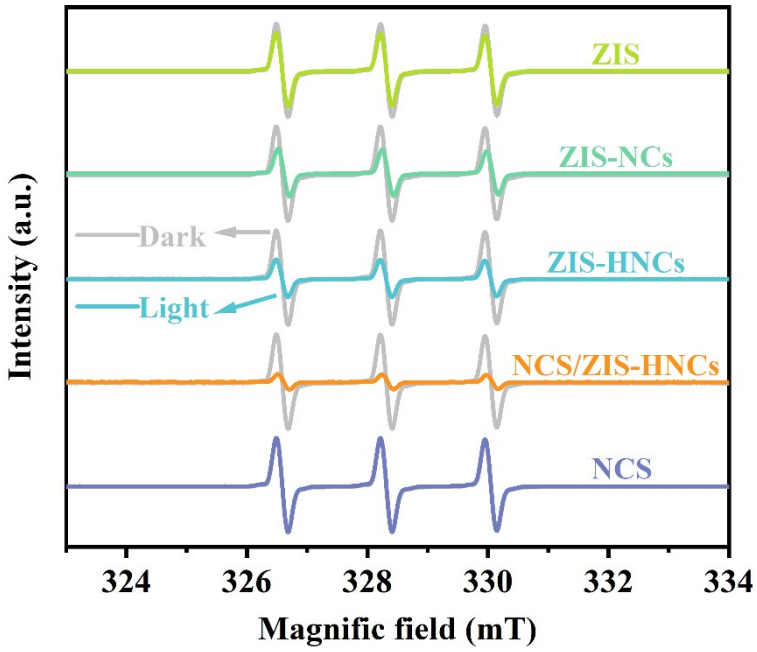

Figure S26. In-situ ESR spectra of the as-synthesized samples (TEMPO-e^-) in the dark and under Xe lamp irradiation.

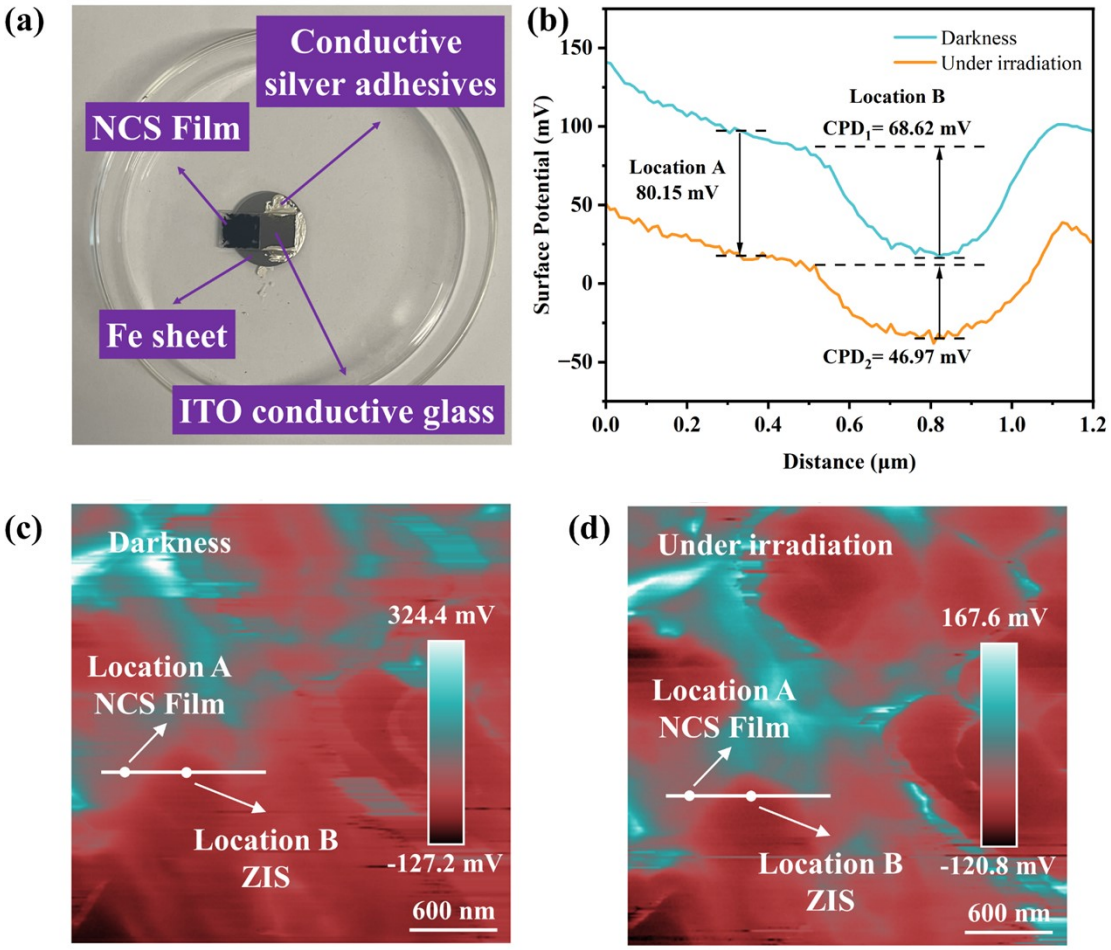

Figure S27. (a) The as-prepared sample for KPFM, (b) Surface photovoltage of NCS-Film/ZIS-HNCs under dark and visible light irradiation, Surface photovoltage distribution of NCS/ZIS-HNCs under darkness (c) and visible-light irradiation conditions (d).

The sample with uniform NCS compact film that ZIS particles dropwise added on it was prepared (**Figure S27a**). The NCS film (location A) exhibits surface potential declines by 80.15 mV under irradiation (**Figure S27b**), indicating the co-catalyst NCS receive photogenerated electrons from ZIS-HNCs. Notably, since the background signals are contributed by NCS film, measuring the contact potential difference (CPD) between ZIS-HNCs and background signals (NCS film) before and under irradiation can evaluate the electron accumulation/consumption of ZIS-HNCs. The CPD of ZIS-HNCs is 68.62 mV before irradiation, and 46.97 mV after irradiation. The decreased CPD indicates the electron consumption of ZIS-HNCs to exhibit relative positive potential. The above result reconfirms the electrons migration form ZIS-HNCs to NCS.

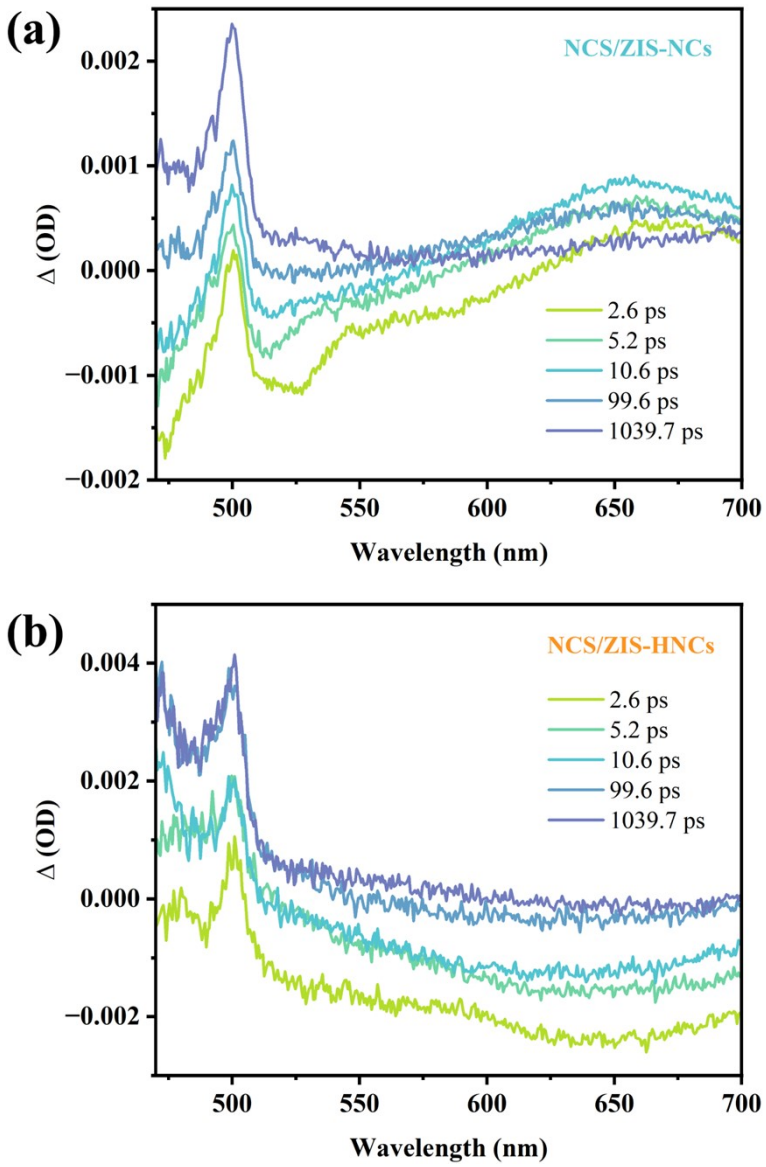

Figure S28. Transient absorption signals of NCS/ZIS-NCs (a) and NCS/ZIS-HNCs (b).

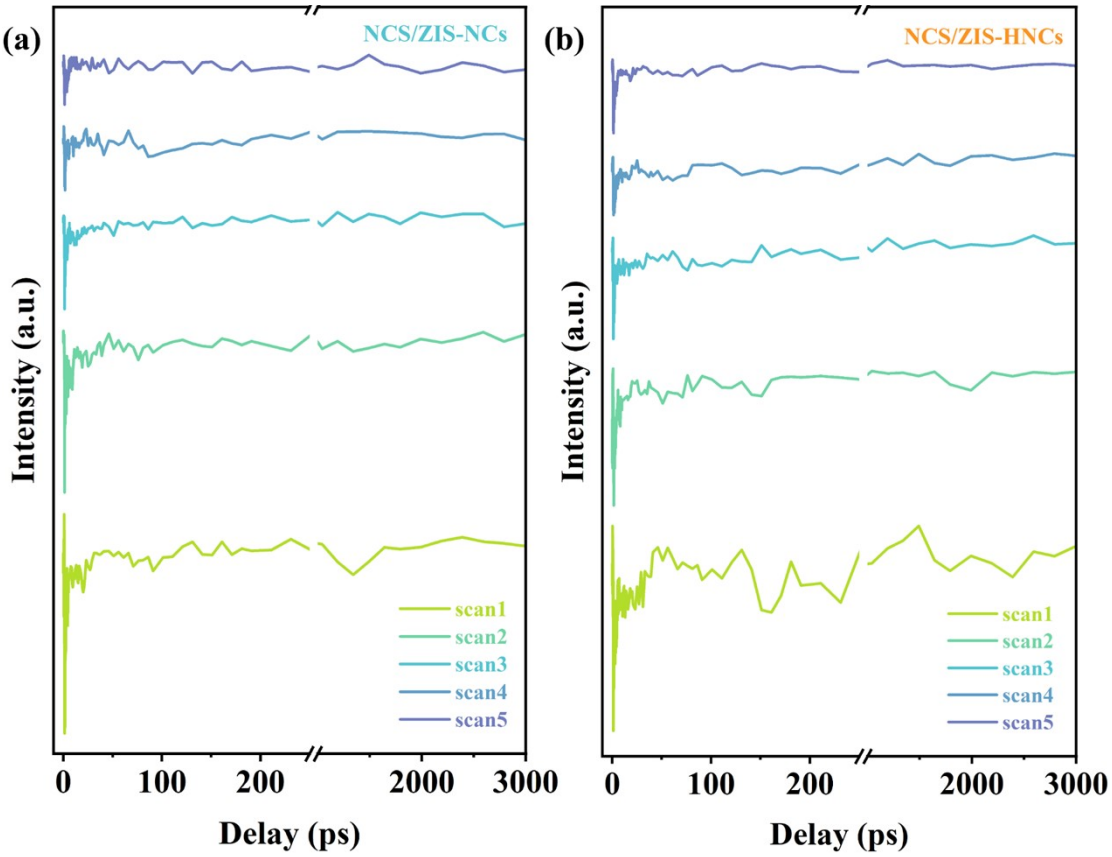

Figure S29. Multiple scans of TAS kinetics probed at 530 nm: (a) NCS/ZIS-NCs and (b) NCS/ZIS-HNCs.

Each test of TAS is scanned five times (**Figure S29**), and the data exhibited in **Figure 5c-d** were averaged over the above five scans using the software of Surface Xplorer shortcut. The lifetimes were obtained by fitting TAS curves with exponential decay function using Origin 2023. The Fitting data of TAS kinetics in **Figure 5c-d** and **Figure S29** are exhibited in **Table S3**.

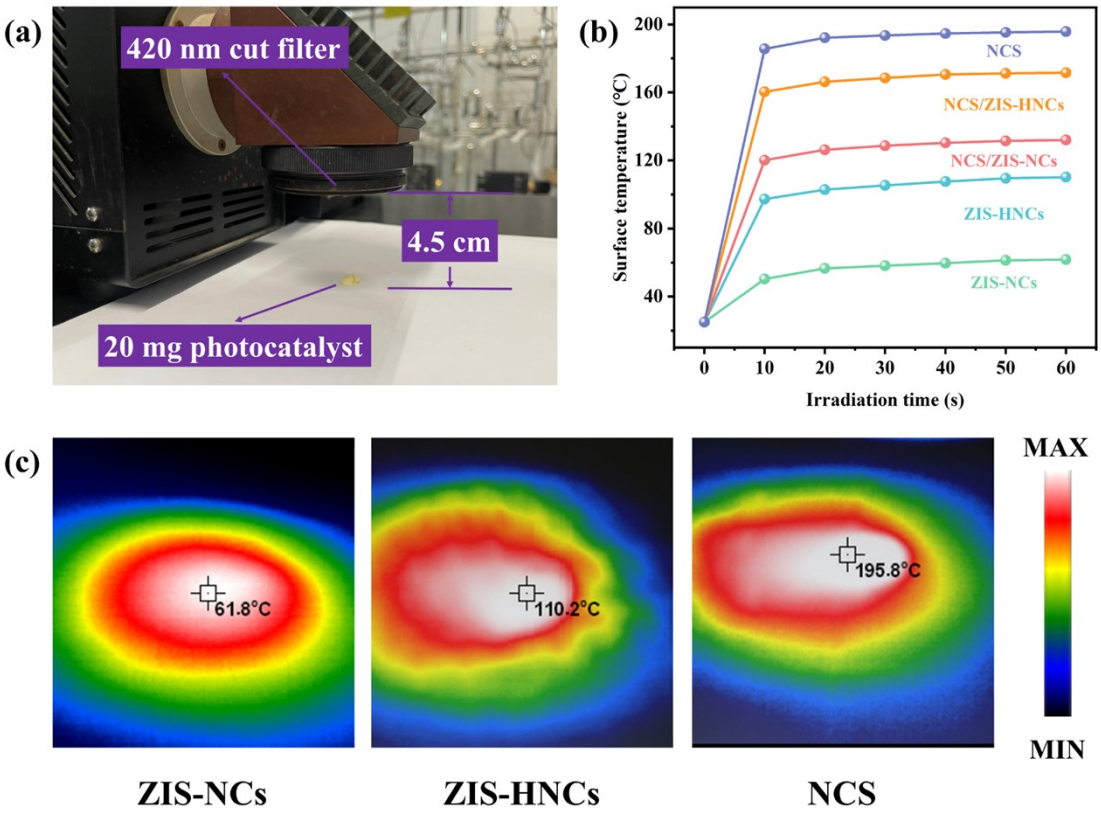

Figure S30. (a) Test environment of surface temperature, (b) Temperature *vs* time curves of the as-synthesized samples within 1 min, (c) Surface temperature of the as-synthesized samples after 1 min irradiation.

The surface temperatures of the as-synthesized photocatalysts were measured by infrared thermal imager (Smart Sensor, ST9450) with 420 nm cut filter (λ > 420 nm) irradiation for 1 min continuously, and 20 mg photocatalyst was placed at 4.5 cm from the lamp cap (**Figure S30a**). The temperature *vs* time curves of the as-synthesized samples exhibit that the temperature gradually stabilizes over time within 1 minute (**Figure S30b**), which is attributed to the heat dissipation of sample in equilibrium with surrounding medium.

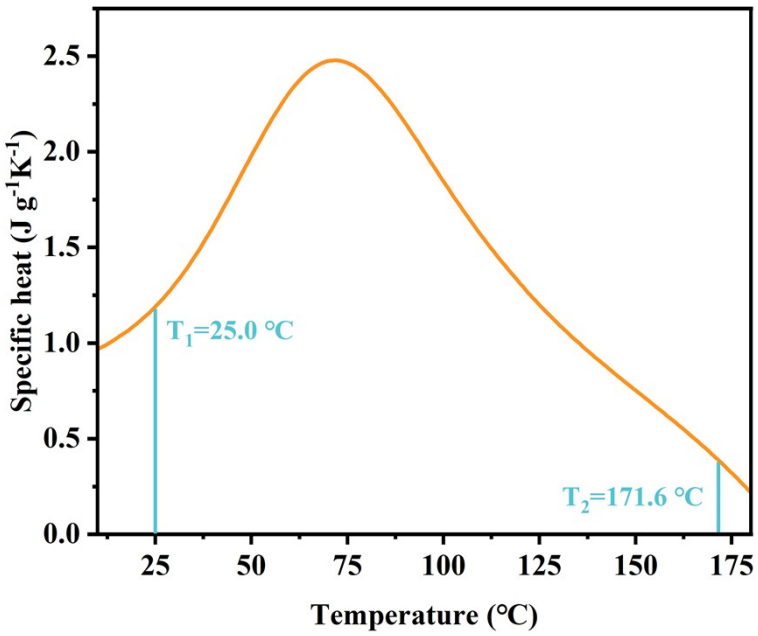

Figure S31. The specific heat *vs* temperature curve of NCS/ZIS-HNCs.

To provide a relatively accurate photothermal conversion efficiency, we calculated the photothermal conversion efficiency of NCS/ZIS-HNCs in the powder state according to the below Equation:

$$\eta = \frac{Q_{thermal\ energy}}{Q_{optical\ energy}} = \frac{m\int_{T_1}^{T_2} cdT}{pt}$$

where m is catalyst quality (0.02 g), $\int_{T_1}^{T_2} cdT$ is curve integral from T_1 (25 ℃) to T_2 (171.6 ℃) in **Figure S31**, p is optical power and t is irradiation time. The specific heat *vs* temperature curve of NCS/ZIS-HNCs was measured by DSC sapphire method (Netzsch dsc 200F3, Germany).

Thus, the photothermal conversion efficiency of NCS/ZIS-HNCs is 6.50% within 1 min. However, since the heat dissipation of sample in equilibrium with surrounding medium, the temperature *vs* time curves of the samples exhibit that the temperature gradually stabilizes over time within 1 minute (**Figure S30b**), the calculated photothermal conversion efficiency decreases gradually over time.

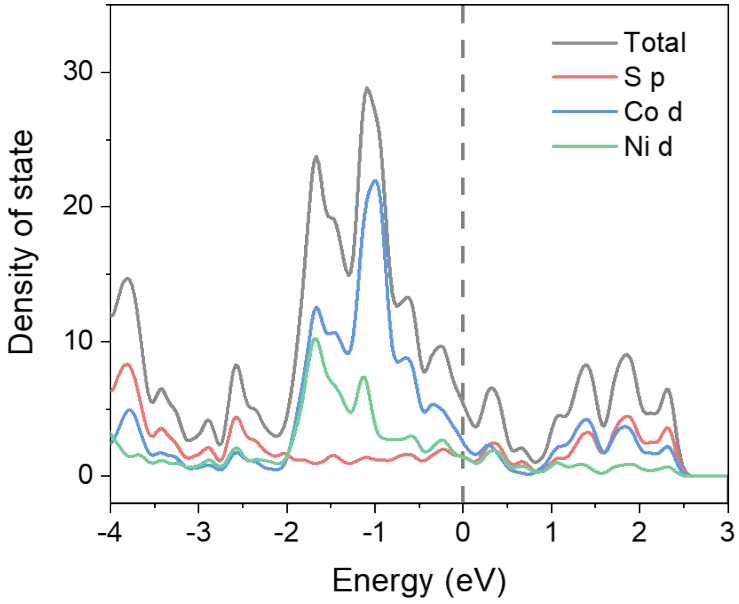

Figure S32. Density of states of NCS.

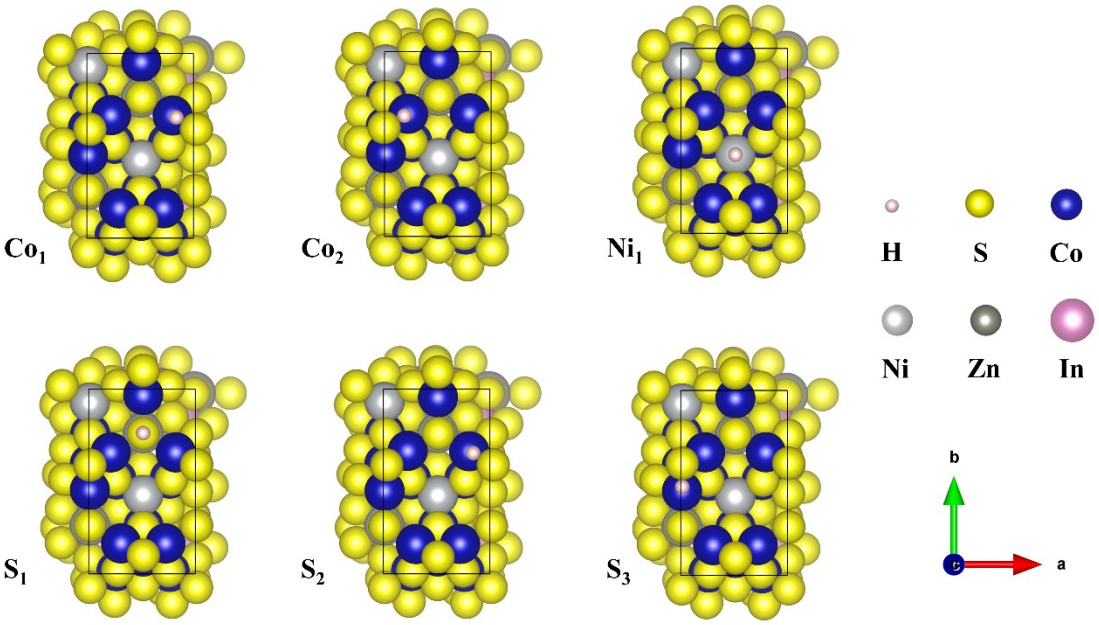

Figure S33. Adsorption of H atom on different sites (HER sites) of NCS in NCS/Vs-ZIS.

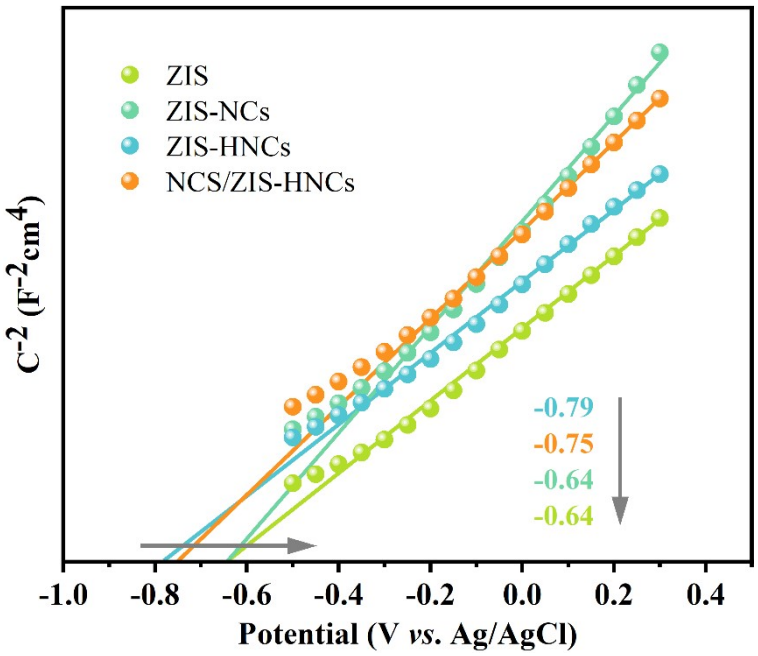

Figure S34. Mott-Schoktty plots of the as-synthesized samples.

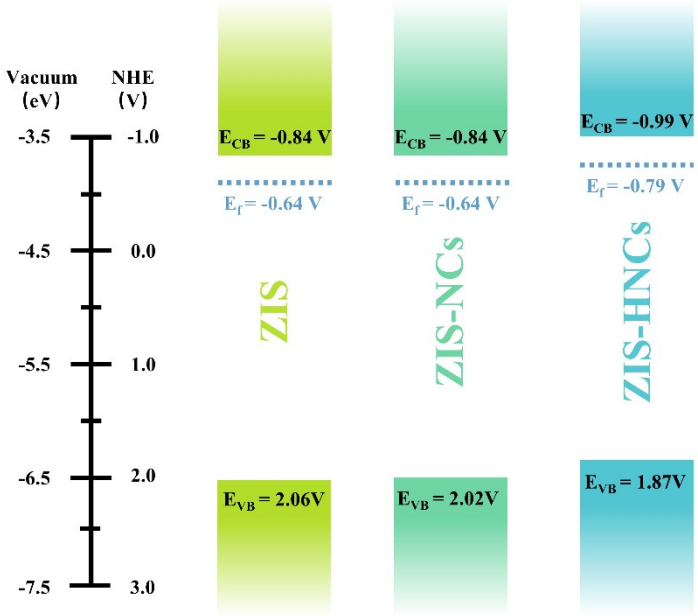

Figure S35. Band structures of the as-synthesized samples.

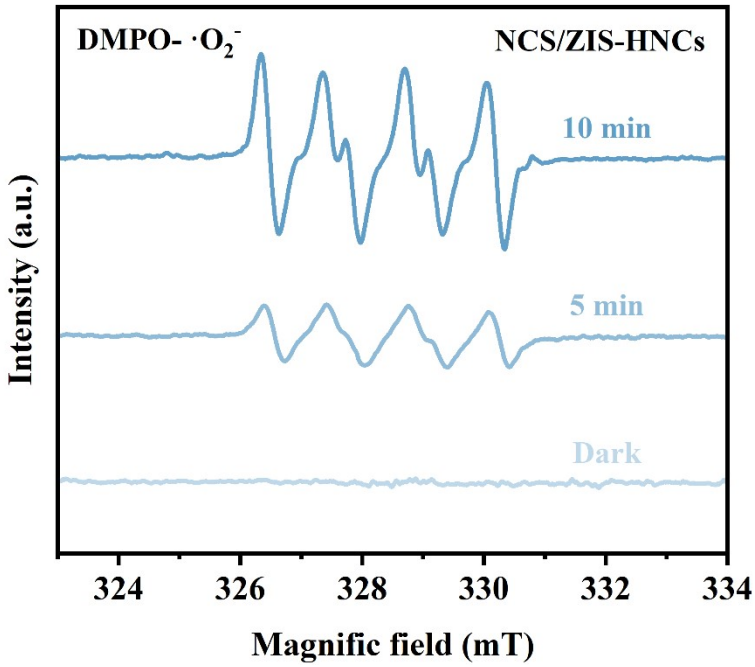

Figure S36. In-situ ESR spectra of the as-synthesized samples (DMPO-·O_2^-).

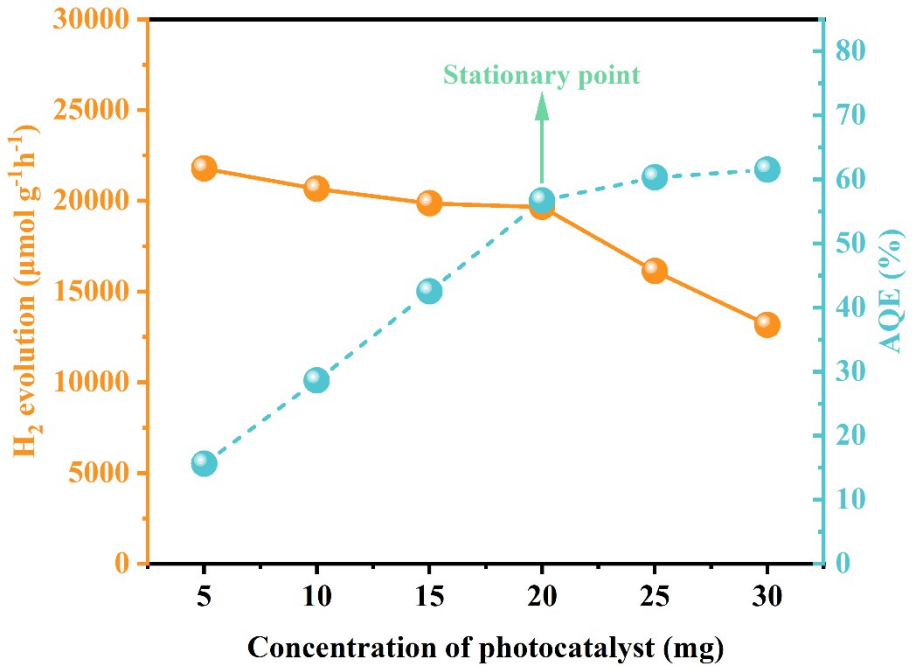

Figure S37. Dependence of the PHE rate under visible light (λ＞420 nm) and AQE value with an optical filter (λ=400 nm) on NCS/ZIS-HNCs photocatalyst concentration.

To expound the rational stationary point for reflecting the PHE rate, both PHE rate under visible light (λ＞420 nm) and AQE value with an optical filter (λ=400 nm) were carried out with different concentration of NCS/ZIS-HNCs photocatalyst (**Figure S37**). When the dosage of photocatalyst exceeded 20 mg, AQE value no longer exhibited a linear increase with the concentration of photocatalyst, while PHE rate exhibited a significant decline due to the optical shielding phenomenon which some of the photocatalyst cannot absorb the light availably. As a result, the optimum mass of NCS/ZIS-HNCs photocatalyst is 20 mg.

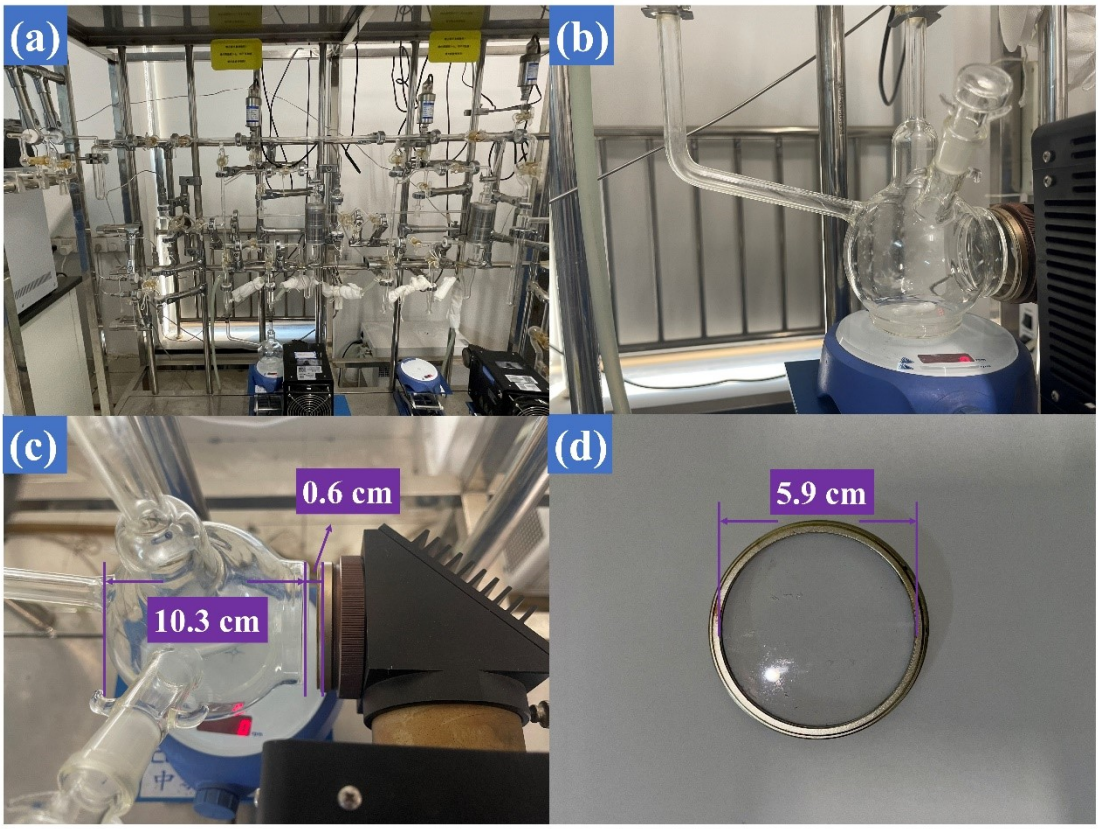

Figure S38. (a) Vacuum system for PHE, (b) Photoreactor for PHE, (c) The length measurement of photoreactor, (d) The length measurement of optical filter.

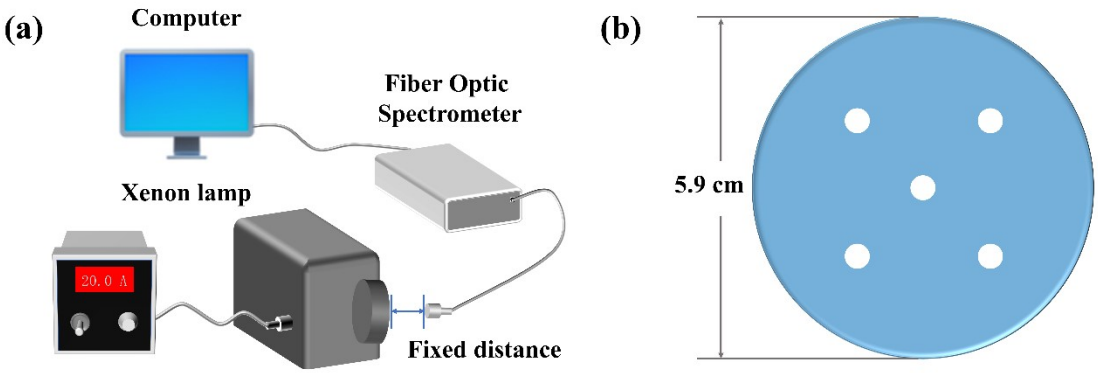

Figure S39. (a) Schematic diagram of light intensity measurement equipment, (b) Five points during the measurement for averaging the light intensity.

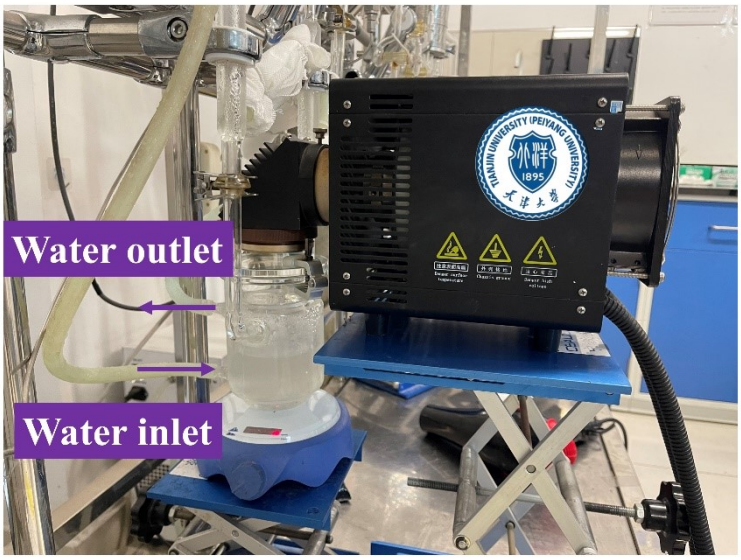

Figure S40. The photoreactor with cooling water.

Table S1. Comparison of photocatalytic hydrogen evolution rate of $ZnIn_2S_4$-based photocatalysts

Photocatalysts	Light (nm)	H_2 evolution rate (μmol/g/h)	AQE	Sacrificial reagents	References
$NiCo_2S_4/ZnIn_2S_4$	**>420**	**19654**	**400 nm 56.7% 420nm 44.2%**	**Ascorbic acid**	**This work**
CoNi-$ZnIn_2S_4$	>420	3333	420 nm 2.15%	Ascorbic acid	9
Cu-$ZnIn_2S_4$	>420	9864	420 nm 37.11%	Ascorbic acid	10
$ZnIn_2S_4$@MoS_2	>420	1162	420 nm 5.09%	Na_2S-Na_2SO_3	11
Pt/Cu-$ZnIn_2S_4$	>420	5020	N/A	Na_2S-Na_2SO_3	12
COP-$ZnIn_2S_4$/Pt	N/A	5040	N/A	Na_2S-Na_2SO_3	13
C/HT-In_2O_3 /$ZnIn_2S_4$	N/A	9366	350 nm 12.18%	Na_2S-Na_2SO_3	14
g-C_3N_4 @$ZnIn_2S_4$	>400	14799	N/A	Na_2S-Na_2SO_3	15
UiO-66@$ZnIn_2S_4$	>420	3062	420 nm 9.84%	TEOA	16
Mxene/$ZnIn_2S_4$	>420	3475	420 nm 11.14%	TEOA	17
$Ni_{1-x}Co_xSe_2C$ /$ZnIn_2S_4$	>420	5100	420 nm 2.32%	TEOA	18
WO_{3-X}/$ZnIn_2S_4$	>400	5769	400 nm 26.28%	TEOA	19
Co_9S_8@$ZnIn_2S_4$	>400	6250	N/A	TEOA	20
Co_9S_8/$ZnIn_2S_4$	>400	9039	420 nm 4.49%	TEOA	21
Co/NGC@$ZnIn_2S_4$	>420	11270	420 nm 5.07%	TEOA	22
Pt-$ZnIn_2S_4$	>420	17500	420 nm 50.4%	TEOA	23

Table S2. Calculated ΔG_{*H} on different sites of NCS/Vs-ZIS in Figure 6b

Position	ΔG_{*H} (eV)	ΔE (eV)	ΔZPE (eV)	$T\Delta S$ (eV)
Co_1	0.56456735	-492.0996191	0.19815	-489.0660364
Co_2	0.55643024	-492.0954462	0.18584	-489.0660364
N_1	1.04001826	-491.6016111	0.175593	-489.0660364
S_1	**0.22762467**	**-492.4545397**	**0.216128**	**-489.0660364**
S_2	0.56301343	-492.099313	0.19629	-489.0660364
S_3	0.54567636	-492.102894	0.182534	-489.0660364
V_S-ZIS	1.78371703	-490.799037	0.11427	-489.068484

Table S3. Fitting data of TAS kinetics in Figure 5c-d and Figure S29

Samples	Scan	τ_1 (ps)	τ_2 (ps)	τ_{av} (ps)	R^2
ZIS-NCs	1	1.17±0.17	32.92±13.84	26.24	0.88
	2	0.10±0.02	7.03±1.05	0.11	0.86
	3	1.10±0.17	43.23±16.17	37.06	0.86
	4	0.98±0.11	354.71±165.11	343.87	0.83
	5	0.27±0.12	4.07±1.06	1.56	0.77
	average	**1.04±0.08**	**30.68±5.88**	**27.09**	**0.97**
ZIS-HNCs	1	0.34±0.08	16.90±3.62	10.06	0.82
	2	2.11±0.25	125.95±43.72	115.40	0.91
	3	1.10±0.09	254.93±66.86	246.35	0.92
	4	2.84±0.29	1406.07±800.68	1397.12	0.90
	5	1.33±0.10	95.89±38.29	82.60	0.94
	average	**1.86±0.12**	**163.57±30.99**	**157.32**	**0.97**

References

1. G. Kresse and J. Furthmüller, *Phys. Rev. B*, 1996, **54**, 11169-11186.
2. J. P. Perdew, K. Burke and M. Ernzerhof, *Phys. Rev. Lett.*, 1997, **78**, 1396-1396.
3. P. E. Blöchl, *Phys. Rev. B*, 1994, **50**, 17953-17979.
4. G. Kresse and D. Joubert, *Phys. Rev. B*, 1999, **59**, 1758-1775.
5. S. Grimme, J. Antony, S. Ehrlich and H. Krieg, *J. Chem. Phys.*, 2010, **132**, 154104.
6. A. D. Becke and E. R. Johnson, *J. Chem. Phys.*, 2007, **127**, 154108.
7. Y. Guo, L. Mao, Y. Tang, Q. Shang, X. Cai, J. Zhang, H. Hu, X. Tan, L. Liu, H. Wang, T. Yu and J. Ye, *Nano Energy*, 2022, **95**.
8. S. Lee, B. Min and J. Bang, *Sci. Rep.*, 2022, **12**, 6076.
9. Z. Li, X. Wang, W. Tian, A. Meng and L. Yang, *ACS Sustain. Chem. Eng.*, 2019, **7**, 20190-20201.
10. S. Zhang, Z. Zhang, Y. Si, B. Li, F. Deng, L. Yang, X. Liu, W. Dai and S. Luo, *ACS Nano*, 2021, **15**, 15238-15248.
11. J. Peng, J. Yang, B. Chen, S. Zeng, D. Zheng, Y. Chen and W. Gao, *Biosens. Bioelectron.*, 2021, **175**, 112873.
12. L. Su, P. Wang, J. Wang, D. Zhang, H. Wang, Y. Li, S. Zhan and J. Gong, *Adv. Funct. Mater.*, 2021, **31**.
13. C. Cui, X. Zhao, X. Su, N. Xi, X. Wang, X. Yu, X. L. Zhang, H. Liu and Y. Sang, *Adv. Funct. Mater.*, 2022, **32**, 2208962.
14. Q. Zhang, J. Zhang, X. Wang, L. Li, Y.-F. Li and W.-L. Dai, *ACS Catal.*, 2021, **11**, 6276-6289.
15. M. Tan, Y. Ma, C. Yu, Q. Luan, J. Li, C. Liu, W. Dong, Y. Su, L. Qiao, L. Gao, Q. Lu and Y. Bai, *Adv. Funct. Mater.*, 2021, **32**, 2111740.
16. X. Peng, L. Ye, Y. Ding, L. Yi, C. Zhang and Z. Wen, *Appl. Catal. B Environ.*, 2020, **260**, 118152.
17. G. Zuo, Y. Wang, W. L. Teo, A. Xie, Y. Guo, Y. Dai, W. Zhou, D. Jana, Q. Xian, W. Dong and Y. Zhao, *Angew. Chem., Int. Ed.*, 2020, **59**, 11287-11292.
18. Y. Chao, P. Zhou, J. Lai, W. Zhang, H. Yang, S. Lu, H. Chen, K. Yin, M. Li, L. Tao, C. Shang, M. Tong and S. Guo, *Adv. Funct. Mater.*, 2021, **31**.
19. D. Luo, L. Peng, Y. Wang, X. Lu, C. Yang, X. Xu, Y. Huang and Y. Ni, *J. Mater. Chem. A*, 2021, **9**, 908-914.
20. S. Wang, B. Y. Guan, X. Wang and X. W. D. Lou, *J. Am. Chem. Soc.*, 2018, **140**, 15145-15148.
21. G. Zhang, D. Chen, N. Li, Q. Xu, H. Li, J. He and J. Lu, *Angew. Chem., Int. Ed.*, 2020, **59**, 8255-8261.
22. S. Wang, Y. Wang, S. L. Zhang, S. Q. Zang and X. W. Lou, *Adv. Mater.*, 2019, **31**, 1903404.
23. X. Shi, C. Dai, X. Wang, J. Hu, J. Zhang, L. Zheng, L. Mao, H. Zheng and M. Zhu, *Nat. Commun.*, 2022, **13**, 1287.